Metals & corrosion

Effect of chromium content on precipitation in Cu–Cr–Zr alloys

Anna Bodyakova[1,2,*] , Roman Mishnev[1], Andrey Belyakov[1], and Rustam Kaibyshev[1]

[1] *Belgorod State University, Pobeda str. 85, Belgorod 308015, Russia*
[2] *National University of Science & Technology (MISIS), Leninsky pr. 4, Moscow 119049, Russia*

ABSTRACT

The phase content and the strengthening of two copper alloys, 0.1Cr–0.1Zr and 0.9Cr–0.1Zr, subjected to aging treatments were studied. The size of second phase particles and the strengthening mechanism depended remarkably on the chromium content. The strengthening of the 0.9Cr–0.1Zr alloy in the peak aged conditions was mainly attributed to the uniform dispersion of tiny shearable Cr-rich particles with a size of about 3–4.5 nm and the Nishiyama–Wassermann orientation relationship. In contrast, the microstructure of the peak aged conditions of the 0.1Cr–0.1Zr alloy was characterized by the dispersion of relatively large Cr particles with a size of about 8–10 nm, which resulted in the strengthening accordingly Orowan mechanism. The reasons for the difference in the decomposition of the supersaturated solid solution and the morphology of particles are discussed.

GRAPHICAL ABSTRACT
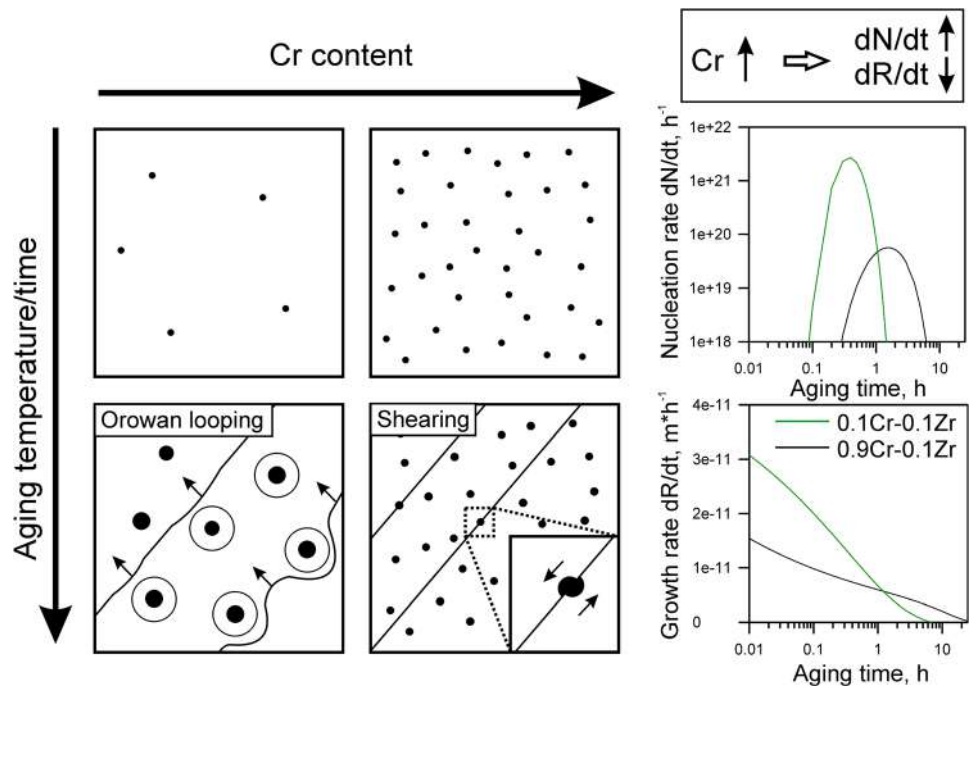
Introduction

Cu–Cr alloys exhibit high strength and high electrical conductivity and are widely used in various electronic devices, contact wires, integral circuits, etc. [1–7]. A good combination of mechanical and physical properties in these alloys can be achieved by conventional heat treatment consisting of solution treatment followed by aging [8–10]. The supersaturated solid solution decomposes during the aging treatment, leading to the precipitation of fine second-phase particles that provide the beneficial strength/conductivity combination. Alloying by Zr, Ti, Mg, etc., is an effective method to improve the mechanical properties of Cu–Cr system alloys. The addition of Ti improves the strength of Cu–Cr alloy owing to the formation of smaller Cr particles and suppression of the particle coarsening [11, 12]. Mg controls the size and fraction of precipitates [13, 14]. The addition of both Ti and Mg to binary Cu–Cr alloy

may significantly harden the alloy, but has a detrimental effect on the electrical conductivity [11–14]. The Cu–Cr–Zr alloy has attracted much attention because of its excellent property combination (electrical conductivity above 80% IACS and tensile strength above 600 MPa). The solubility of Cr and Zr in Cu–Cr–Zr alloys at room temperature is very low (less than 0.03% for Cr and 0.01% Zr). Thus, Cr and Zr atoms will precipitate out from the supersaturated solid solution, resulting in particle strengthening and enhancing the electrical conductivity [8–10].

Specific attention was paid to understanding the phase composition of the binary Cu–Cr and Cu–Zr copper alloys in a Cu-rich corner of the phase diagram [1, 8, 15–19]. Fine Cr dispersoids with body-centered cubic (bcc) structure usually precipitate from the solid solution [8, 20, 21], although some authors suppose that Cr dispersoids could have a metastable face-centered cubic (fcc) structure at an early age [2, 8, 22] that can be considered as Cr-enriched areas of the Cu lattice. The coherent platelet

[22] and rod-shaped [23] Cr particles were observed. Additionally, the Cr particles were described as Guinier–Preston (GP) zones with a size of several atoms [1]. Moreover, Cr dispersoids with such shapes as ellipsoid [15], sphere [24] and hexagon [25] were reported. The binary Cu–Zr system is characterized by a large number of second-phase particles, such as Cu_3Zr with a hexagonal close-packed (hcp) structure [26], fcc Cu_5Zr [27–29], and orthorhombic Cu_4Zr or Cu_9Zr_2 phase [30–32].

Despite several works devoted to examining the phase composition in Cu–Cr–Zr alloys after aging treatment, the crystal structure and phase stoichiometry remain a subject of some debate. The formation of ordered fcc Cr-rich particles was reported for an early stage of decomposition of the supersaturated solid solution [2]. Then, the fcc Cr-rich particles transformed to the Cr precipitates with bcc B2-type structure. In addition to the Cr precipitates in the peak aged conditions, the Heusler phase of $CrCu_2$ (Zr, Mg) was found in a Cu–Cr–Zr–Mg alloy [1, 33]. An overaging was reported to result in the decomposition of Heusler phase into two phases: the first, the Cr-rich phase having stable bcc structure, and the second, Cu_4Zr phase having an orthorhombic lattice [33–35]. In addition to the fine second phase dispersoids, the coarse Zr and Cr particles could also be observed.

Note that most studies dealt with Cu–Cr–Zr alloys with Cr content of more than 0.5 weight % [10–12, 17–22, 33–35], and only some works discussed the phase transformation in Cu-0.2%Cr-X. Nishiyama–Wassermann and Kurdyumov–Sachs orientation relationships between bcc Cr particles and copper matrix were observed by Fujii et al. at early aging [15]. After prolonged aging, only Kurdyumov–Sachs orientation relationship remained [15]. On the other hand, Wang et al. reported two types of dispersed particles: fcc Cr with a size of 3.5 nm and bcc Cr with a size of 10.6 nm [36]. The precipitation behavior of Cu–Cr–Zr alloys with the same content of Cr and Zr has not been detailed, although such alloys exhibit attractive properties, e.g., a Cu-0.1%Cr-0.1%Zr is characterized by thermal stability up to 500 °C and the strength above 450 MPa along with the electrical conductivity above 90% IACS after appropriate thermomechanical treatment [37–39]. Clarification of the phase composition of ternary Cu–Cr–Zr alloys and the effect of Cr content on the particle precipitation are important for determining the optimal heat treatment conditions as well as for predicting the mechanical/electrical properties. Therefore, the main aim of this work is to clarify the phase composition in two ternary Cu–Cr–Zr alloys with different chromium contents.

Regarding the contribution to the mechanical properties, the major role is played by the fine Cr phase particles [16, 20, 40]. The nanoscale dispersoids play a role of obstacles for the dislocation motion [40, 41]. There are two types of interaction between precipitates and dislocations [41]. One of them is the well-known Orowan mechanism, when the dislocations produce loops around the precipitates [42, 43], leading to the precipitation strengthening, σ_{OR},

$$\sigma_{OR} = 0.84MGb/\lambda, \tag{1}$$

where M is the Taylor factor, G is the shear modulus, b is Burger's vector, and λ is the interparticle distance. The other type of interaction is the shearing of the precipitates by dislocation [41, 44–48]. In this case, the process of interaction can be considered as a sum of chemical strengthening, modulus strengthening, coherency strengthening, and other factors [44–48]. Taking into account the precipitation strengthening, the Hall–Petch relationship can be modified as follows:

$$\sigma_{YS} = \sigma_0 + \sigma_p + k_y d^{-0.5} + \sigma_\rho, \tag{2}$$

where σ_0 is the yield strength of the alloy without grain boundaries and particles, d is the grain size, k_y is the Hall–Petch coefficient, σ_p is the precipitation strengthening, σ_ρ is the dislocation strengthening. The mechanisms of precipitation strengthening and the contribution of fine precipitates to the mechanical properties of Cu–Cr–Zr alloys remain unclear. Therefore, this work is also aimed to estimate the contribution of fine dispersoids to the yield strength of copper alloys with different chromium contents.

Materials and experimental procedure

Two copper alloys, 0.1Cr–0.1Zr and 0.9Cr–0.1Zr, with chemical compositions of 0.096 wt.% Cr, 0.07 wt.% Zr, Cu—balance and 0.87 wt.% Cr, 0.06 wt.% Zr, Cu—balance, respectively, were investigated. The alloys were fabricated by direct chill casting. The solution treatment was conducted at a temperature of 920 °C for 1 h, followed by water quenching. Then, the samples were subjected to aging in a temperature

range of 200–700 °C for 1 h. Several samples were aged at temperatures of 450, 500, and 550 °C for 0.5 h to 16 h.

The hardening was studied by microhardness tests using a WOLPERT 420 MVD device with a load of 300 g and a dwell time of 10 s. The electrical conductivities of the samples were measured by an eddy current method using a Constant K6 device. The samples for microhardness tests and conductivity measurements were subjected to a two-step polishing, with an initial polishing on 1000-grit SiC paper followed by a final polishing on a diamond suspension containing diamond particles with a size of 3 μm. The mechanical tests were conducted at room temperature using an Instron 5882 tensile machine. The specimens with a 12 mm gauge length and 1.5 mm × 3 mm cross section were tested at an initial strain rate of 2×10^{-3} s^{-1}.

The precipitates and the fine microstructures were investigated by a transmission electron microscope (TEM), Jeol JEM-2100, operating at 200 kV. The number density of particles was measured on TEM images as particle number per unit area, counting at least 300 particles for each aging condition. The dislocation density was evaluated by counting the individual dislocations on at least 5 typical TEM images. TEM samples were prepared by the twinjet polishing method (Tenupol 5, Struers) at −25 °C using an electrolyte with a chemical composition of 750 ml CH$_3$OH and 250 ml HNO$_3$.

Results

Isochronal aging

Figure 1a and c shows the changes in the hardness and the electro-conductivity as functions of temperature under conditions of isochronal aging during 1 h. The hardness increases significantly with temperature in the range of 300–450 °C, attaining a maximum of 92 HB at 450–475 °C for the 0.9Cr–0.1Zr alloys. Then, the hardness decreases after aging at temperatures above 500 °C. Similar behavior of the hardness change is observed for the 0.1Cr–0.1Zr alloy. The hardness increases progressively with increasing aging temperature and reaches a maximum of approximately 67 HB after aging at 550 °C for 1 h followed by a decrease in hardness with further increase in aging temperature. An increase in the

aging temperature above 350 and 450 °C leads to a rapid increase in the electro-conductivity in the 0.9Cr–0.1Zr and 0.1Cr–0.1Zr alloys, respectively. The maximum of electro-conductivity of 93 and 87% IACS is correspondingly achieved after aging at 550 and 600 °C in the 0.9Cr–0.1Z and 0.1Cr–0.1Zr alloys. Then, the electro-conductivity gradually decreases after aging at temperatures above 600 °C.

Isothermal aging

The influence of aging time on the hardness and the electro-conductivity of the 0.1Cr–0.1Zr and 0.9Cr–0.1Zr alloys are shown in Fig. 1b and d. For comparison, the influence of aging time was studied at temperatures of 450–550 °C for 0.1Cr–0.1Zr and 450–550 °C for 0.9Cr–0.1Zr alloy. (The temperatures expected to result in maximal strengthening were selected.) Following an increase to a maximum, the hardness of the 0.1Cr–0.1Zr alloy slightly decreases, approaching some saturation value with increasing the aging time. The hardness level depends sensitively on the aging temperature in the 0.1Cr–0.1Zr alloy. It should be noted that an increase in the aging temperature from 450 °C to 550 °C shifts the peak hardness to a shorter aging time. The hardness curves for the 0.9Cr–0.1Zr alloy are characterized by almost the same shape. Aging leads to reaching the hardness maximum of about 90–105 HB irrespective of the aging temperature. The hardness level decreases by about 5–10 HB with an increase in aging temperature by about 50 °C.

Aging at 450 °C is accompanied by a gradual increase in electrical conductivity of the 0.1Cr–0.1Zr to 75% IACS after 16 h. An increase in aging temperature to 500 or 550 °C increases the maximum (saturation level) electro-conductivity to 93% IACS, while the period to saturation comprises 12 or 6 h, respectively. The electrical conductivity of the 0.9Cr–0.1Zr alloy after aging at 450–500 °C for 8 h achieves 90% IACS and then stabilizes. Aging at 550 °C for 0.5 h of the 0.9Cr–0.1Zr alloy leads to significant increase in the electrical conductivity above 90% IACS.

Mechanical properties

The engineering stress–strain curves of the Cu–Cr–Zr alloys in the solution-treated (ST) and peak-aged conditions are presented in Fig. 2. The stress–strain

Figure 1 The effect of aging temperature (**a**, **b**) and time (**c**, **d**) on the hardness (**a**, **c**) and electro-conductivity (**b**, **d**) of 0.9Cr–0.1Zr (green symbols) and 0.1Cr–0.1Zr (black symbols) alloys.
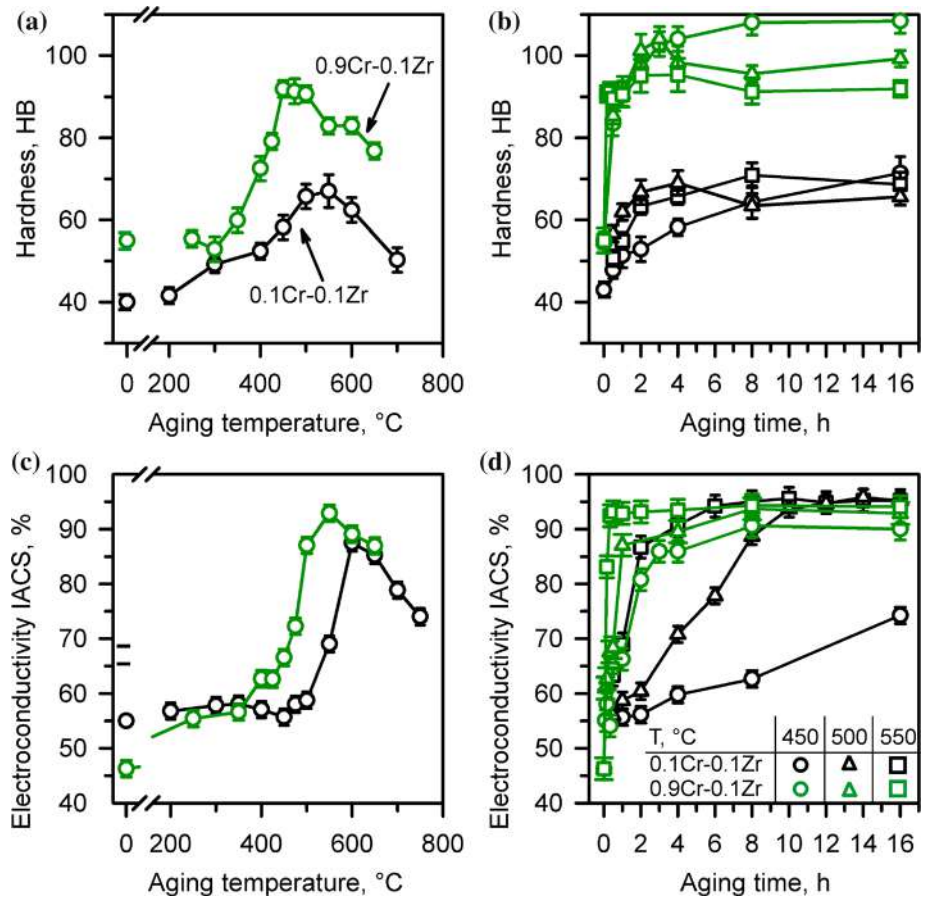
Figure 2 Engineering stress–strain curves obtained by tensile testing of 0.9Cr–0.1Zr (**a**) and 0.1Cr–0.1Zr (**b**) alloys after aging at a temperature of 450 °C, 500 °C, or 550 °C.
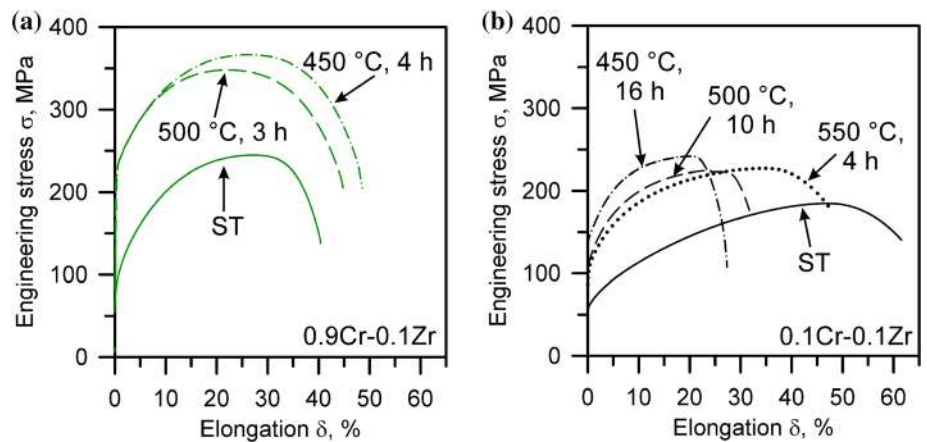
curves are characterized by a rapid strain hardening during early deformation. Then, the rate of strain hardening gradually decreases leading to a stress maximum followed by a progressive decrease in the flow stress until rupture. In the solution-treated conditions, the 0.9Cr–0.1Zr alloy exhibits higher ultimate tensile strength (UTS) of approximately 240 MPa, comparing with 185 MPa for the 0.1Cr–

0.1Zr. Aging treatment of the 0.9Cr–0.1Zr alloy results in more than 100 MPa increment in the UTS. The yield strength (YS) increases from 80 MPa in the initial state to 215 MPa after aging at 450 °C for the 0.9Cr–0.1Zr alloy. Note here that UTS in the 0.9Cr–0.1Zr alloy increases simultaneously with total elongation. In contrast, aging treatment of the 0.1Cr–0.1Zr alloy does not result in such a remarkable change in

the tensile properties. YS and UTS increase from 60 and 185 MPa in the initial state to approximately 120–140 and 220–230 MPa, respectively, regardless of the aging temperature in the range of 450–550 °C. Total elongation in 0.1Cr–0.1Zr alloy decreases after aging.

Particle precipitation

The dispersed particles in the 0.1Cr–0.1Zr alloy after aging at 450 °C are presented in Fig. 3a–d. The decomposition of solid solution in the 0.1Cr–0.1Zr alloy after 1 h aging is barely visible, sparse particles

with a size of about 4 nm are observed in the dark-field TEM image (Fig. 3a). An increase in aging time to 4 h results in the formation of Cr-rich particles with coffee-bean contrast and a size of about 4.5 nm in 0.1Cr–0.1Zr alloy. The precipitations do not exhibit any reflections on the corresponding diffraction pattern due to, probably, low volume fraction of about $\sim 10^{-5}$ of Cr-rich precipitates. Aging for 16 h promotes precipitation in the 0.1Cr–0.1Zr alloy, the bcc-Cr particles elongate along $< 110 >$ in Cr corresponding to $< 001 >$ in Cu. The corresponding SAED patterns reveal individual reflexes from the bcc-Cr lattice. The SAED patterns suggest the Bain
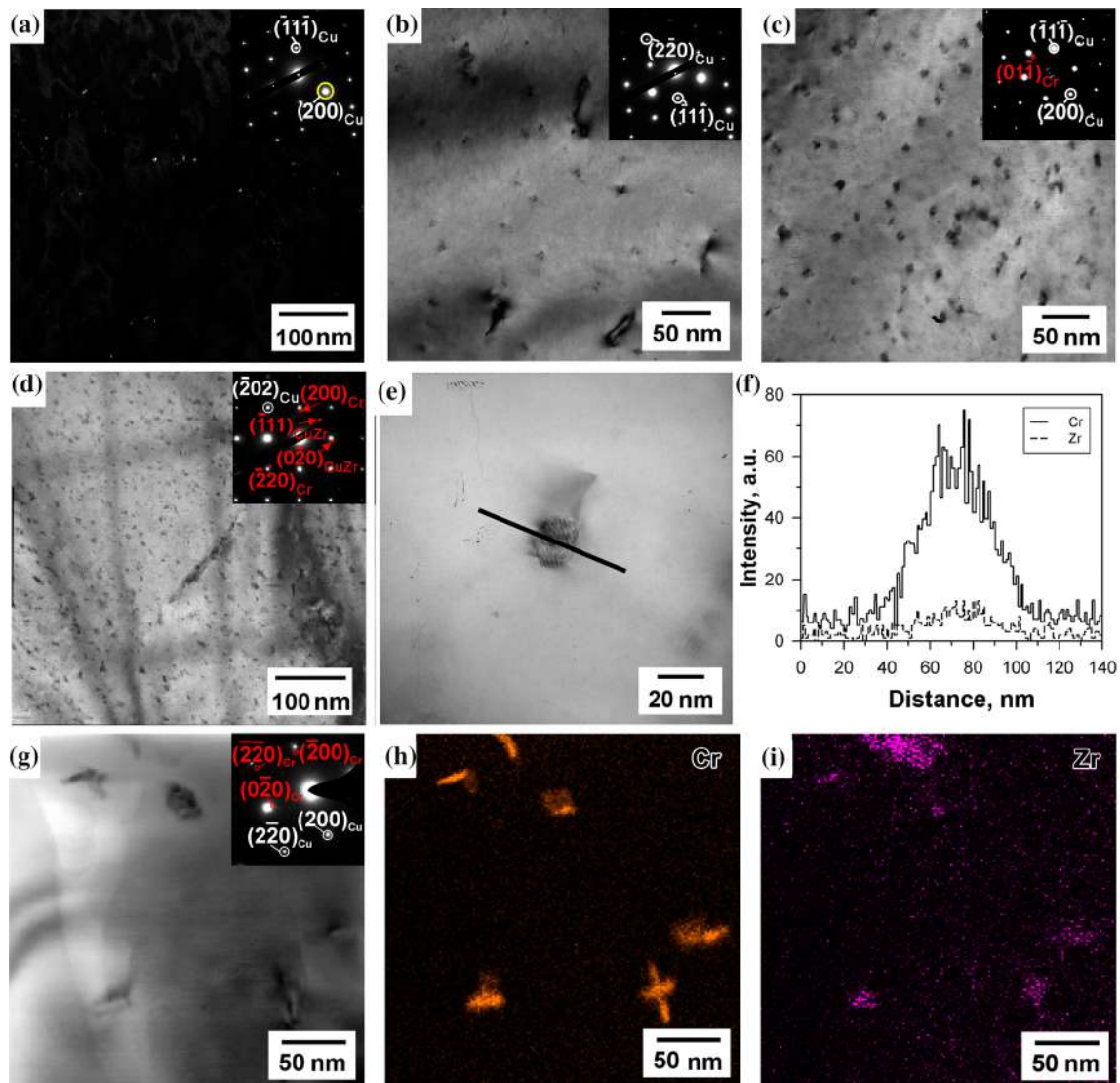
Figure 3 The fine microstructure of the 0.1Cr–0.1Zr alloy after aging at 450 °C for 1 h (**a**), 4 h (**b**), 16 h (**c**), 24 h (**d**) and after aging at 550 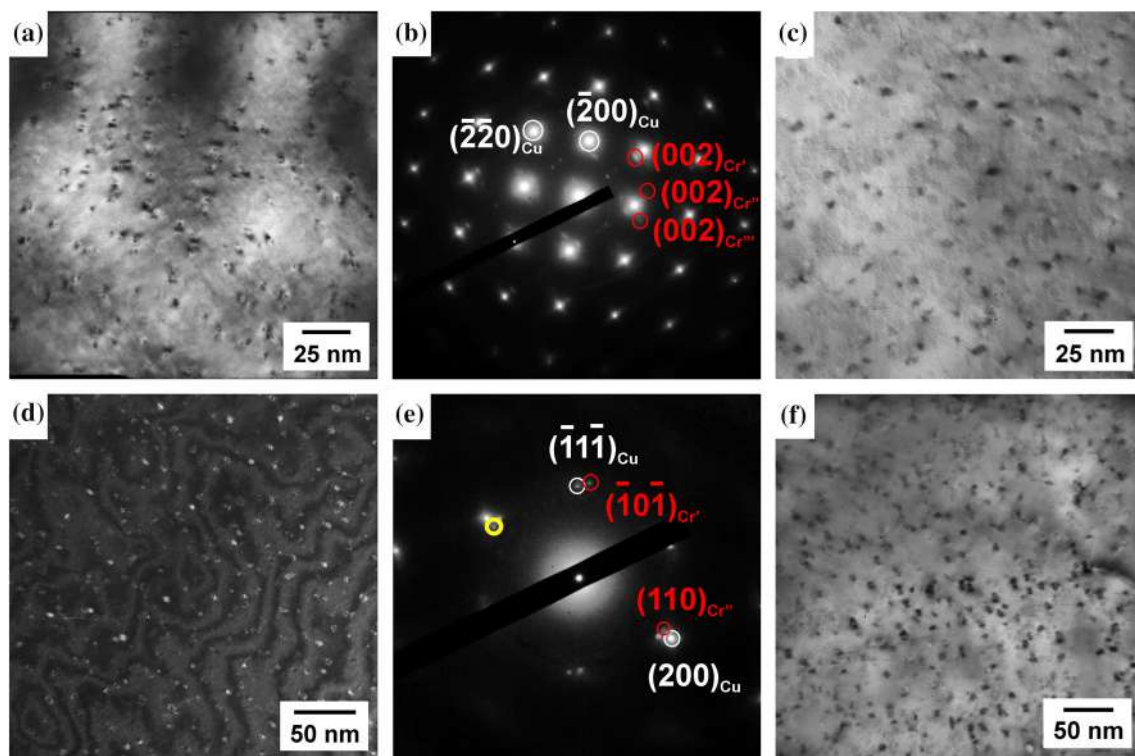°C for 4 h (**e**) to (**k**). Weak-beam dark-field image in (**a**) was obtained from the scattered beam marked by yellow circle. **f** Shows the distribution of Cr and Zr across the particle in (**e**), and (**h**) and (**k**) show the distributions of Cr and Zr in (**g**), respectively.

orientation relationships (OR) between the Cr_{bcc} and Cu_{fcc} crystal lattice, i.e., $(200)_{Cu}(200)_{Cr}$, $[010]_{Cu}[01–1]_{Cr}$. The longitudinal size of bcc-Cr achieves 7 nm and the transverse dimension is 6 nm. New Zr-rich particles with hexagonal lattice with a c/a ratio of about 1.76 and lattice parameters of $a = 0.203$ nm and $c = 0.357$ nm are observed in the 0.1Cr–0.1Zr alloys after 24 h of aging. The rod-like Zr-particles aligned along $< 011 >$ in matrix have a longitudinal size of about 50 nm and a transverse dimension of 5 nm. The size of elongated precipitates after peak aging at a temperature of 550 °C is approximately 15 nm (Fig. 3e–j). The particles are characterized by a bcc-Cr lattice with Bain OR. Figure 3e–j shows detailed chemical analysis of individual particles. It is seen that both Cr and Zr are concentrated within the same particles.

The products of solid solution decomposition after aging at 450 and 500 °C for the 0.9Cr–0.1Zr alloy are shown in Fig. 4. Numerous tiny particles with an average size of approximately 4 nm are homogeneously distributed in the copper matrix in the 0.9Cr–0.1Zr alloy after aging for 4 h at 450 °C. These particles are characterized by an almost spherical shape and coffee-bean contrast. The line of no contrast coincides with approximately $< 001 >$ matrix direction. The corresponding SAED patterns reveal individual reflexes from bcc-Cr lattice typical for Nishiyama–Wassermann (N–W) OR, i.e., $(111)_{Cu}(1–10)_{Cr}$, $[–101]_{Cu}[001]_{Cr}$ for early state of Cr-particle precipitation. Prolonging the aging at 450 °C is accompanied with sluggish coarsening of chromium dispersoids. The average particle size increases to 4.5 nm after aging for 16 h. Aging at 500 °C also leads to precipitation of bcc-Cr dispersoids exhibiting N–W OR. The size of these particles comprises 5–6 nm after aging for 3–16 h. Note here that the shape of dispersoids somewhat changes from a spherical shape after aging at 450 °C to an elongated shape after aging at 500 °C.

In addition to nanosized Cr-rich particles, many relatively coarse particles are observed in the aged 0.9Cr–0.1Zr samples (Fig. 5). These coarse particles are probably primary precipitates that were not dissolved during the solution treatment. The coarse particles can be grouped into two categories,

Figure 4 The fine microstructure of the 0.9Cr–0.1Zr alloy after aging at 450 °C for 4 h (**a**), 16 h (**c**), and after aging at 500 °C for 3 h (**d**), 16 h (**f**). The diffraction patterns in (**b**) and (**e**) correspond to the images in (**a**) and (**d**). Weak-beam dark-field image was obtained from the scattered beam marked by yellow circle in (**e**).

Figure 5 The fine microstructure of the 0.9Cr–0.1Zr after aging at 450 °C for 1 h (**a**) and for 16 h (**b**), and after aging at 500 °C for 0.5 h (**c**) and for 3 h (**d**). The chemical compositions in tables are shown in atomic pct. for the indicated areas.
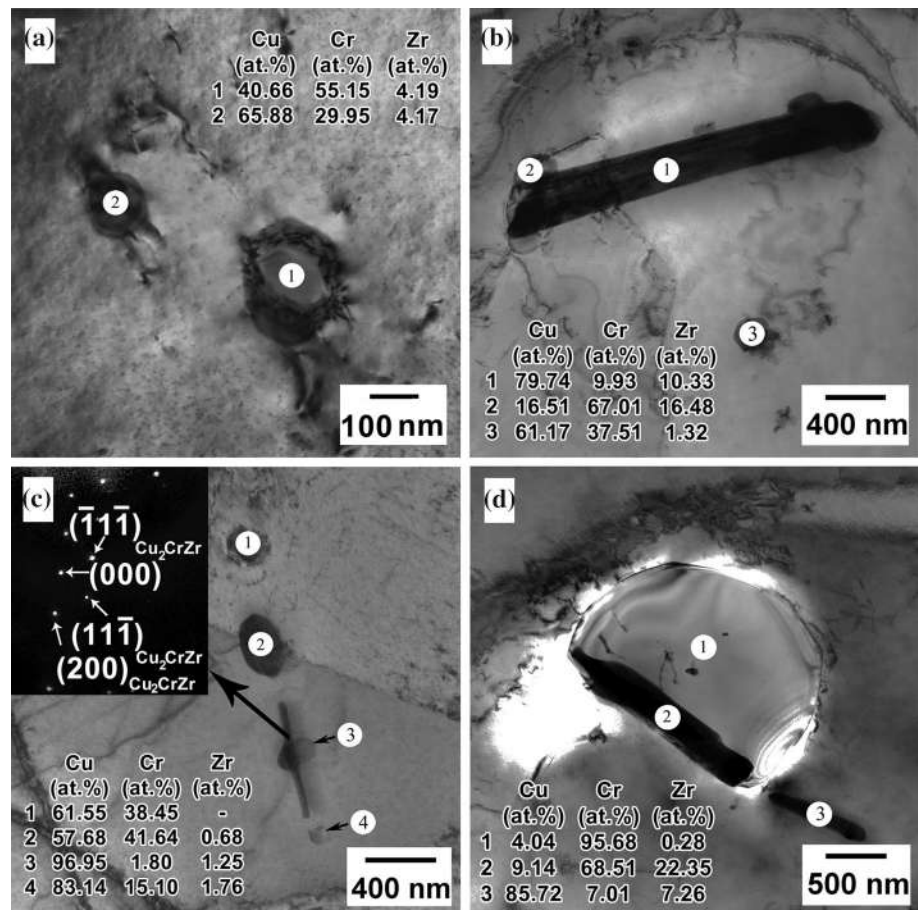

depending on the Zr content. Those are chromium particles containing a small amount of Zr (typically below 20%) and particles containing equal atomic fractions of Cr and Zr. The chromium particles are characterized by an almost spherical shape, and the size of the particles varies from 100 to 500 nm. Other particles, i.e., Cr–Zr particles, are elongated rectangular plates with a length above 1 μm. The stoichiometry of this phase is similar to the Heusler phase, $CrCu_2(Zr, Mg)$ [1, 29]. The SAED patterns obtained from the relatively coarse elongated particles suggest that this phase can be considered as a Heusler phase with a lattice parameter of a = 0.597 nm [49].

The number of particles on a unit square and the particle size are represented in Fig. 6 as functions of

Figure 6 Influence of aging time and aging temperature on the number density N_s (**a**) and the size D_{part} (**b**) of Cr particles in the 0.1Cr–0.1Zr (black symbols) and 0.9Cr–0.1Zr (green symbols) alloys.
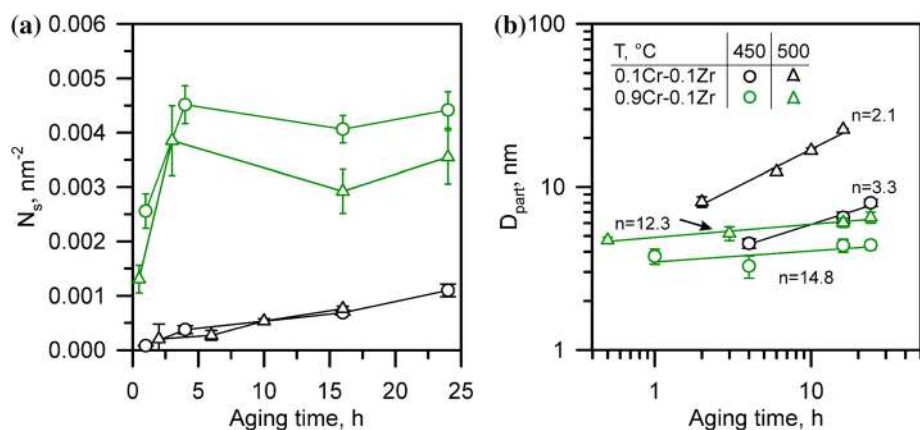
temperature and aging time. An appearance of isolated dispersed particles in the 0.1Cr–0.1Zr alloy after short aging times correlates with the incubation period in the electrical conductivity change. The number density of particles increases gradually with aging time in the 0.1Cr–0.1Zr alloy. In contrast, the number density of dispersed particles with coffee-bean contrast twofold increases in the 0.9Cr–0.1Zr alloy with an increase in aging time from 0.5–1 h to 3–4 h and then does not vary remarkably with further aging.

The particle stability against coarsening depends remarkably on the chromium content. The products of the decomposition of the solid solution in the 0.1Cr–0.1Zr alloy are coarser in comparison with the 0.9Cr–0.1Zr alloy. The size of fine Cr-rich particles in the 0.9Cr–0.1Zr alloy does not significantly depend on the aging temperature and time. Upon increasing the aging time from 1 to 24 h, the average precipitate size increases from 4 to 4.5 nm at 450 °C and from 5 nm to 6.5 nm at 500 °C. Correspondingly, a rather large value of particle growth exponent of about 12–15 is observed (Fig. 6b). In contrast, the size of Cr particles in the 0.1Cr–0.1Zr alloy rapidly increases during aging. The size of the Cr precipitates changes almost twofold from 4 to 8 nm as the aging time increases from 1 to 24 h at a temperature of 450 °C. At an early stage of aging at 500 °C, the mean size of the precipitates reaches almost 8 nm. Further increase in aging time to 16 h is accompanied by coarsening of the precipitates to 23 nm. The grain growth exponent decreases from 4.7 to 2.1 as the aging temperature increases from 450 to 500 °C (Fig. 6b).

Discussion

Solid solution decomposition

The behavior of the decomposition of supersaturated solid solution in the present alloys depends on the alloying extent. TEM observations suggest that the particle precipitation occurs readily in the 0.9Cr–0.1Zr alloy after aging at relatively low temperature. Cr-particles with N–W orientation relationship are characterized by small size, high volume fraction, and significant resistance to growth during aging (Fig. 4). Reducing the Cr content in Cu–Cr–Zr alloy to 0.1% leads to the change in the decomposition

kinetics and the particle morphology. The precipitation takes place after long aging at 450 °C (Fig. 3c–d). The particles in the 0.1Cr–0.1Zr alloy are differentiated by orientation relationship, relatively large size, and small volume fraction. Zel'dovich et al. also reported that the particle size in a Cu–0.14Cr–0.04Zr alloy is smaller than in a Cu–0.09Cr–0.08Zr alloy, despite that the chromium concentration is higher after aging at the same temperature and time [19].

The deceleration of the solid solution decomposition with a decrease in Cr content is confirmed by the electrical conductivity variation with aging time and temperature (Fig. 1). The electrical resistivity (inverse to electrical conductivity) significantly changes with aging temperature and time due to reduction in electron scattering on the atoms of alloying elements. Mattison proposed to use the electron relaxation time for the estimation of electrical resistivity [50]. According to Mattison's equitation, the fraction of solid solution decomposition can be expressed as [4, 7]:

$$f_{\text{decomp}} = \frac{\Omega_0 - \Omega_i}{\Omega_0 - \Omega_{\min}}, \tag{3}$$

where Ω_0 is the electrical resistivity after solution treatment, Ω_i is the current electrical resistivity, $\Omega_{\min}$ is the electrical resistivity in the thermodynamic equilibrium condition.

The decomposition of solid solution in conductive materials can be expressed by a sigmoid law function as [51]:

$$f_{\text{decomp}} = 1 - \exp(-At^k), \tag{4}$$

where f_{decomp} is a fraction of decomposition of the supersaturated solid solution, A is a constant characterizing the incubation period of the particle precipitation, k is a constant that is associated with the rate of the decomposition of solid solution.

Conversion of Eqs. (3) and (4) leads to:

$$\ln \ln \left(\frac{1}{1 - f_{\text{decomp}}} \right) = \ln A + k \ln t. \tag{5}$$

This relationship is illustrated in Fig. 7. The plots of $\ln \ln (\frac{1}{1 - f_{\text{decomp}}})$ vs $\ln t$ represent straight lines with different slopes. All data points of the 0.1Cr–0.1Zr alloy aged at temperatures of 450–500 °C are well described by linear regression with a slope of $k = 1.3$–1.4 (Fig. 7a). An increase in aging temperature to 550 °C leads to splitting data into two groups with a slope of

Figure 7 Kinetic of decomposition of solid solution (**a**) and the fraction of decomposition of solid solution (**b**) of the 0.9Cr–0.1Zr (green symbols) and 0.1Cr–0.1Zr (black symbols) alloys.
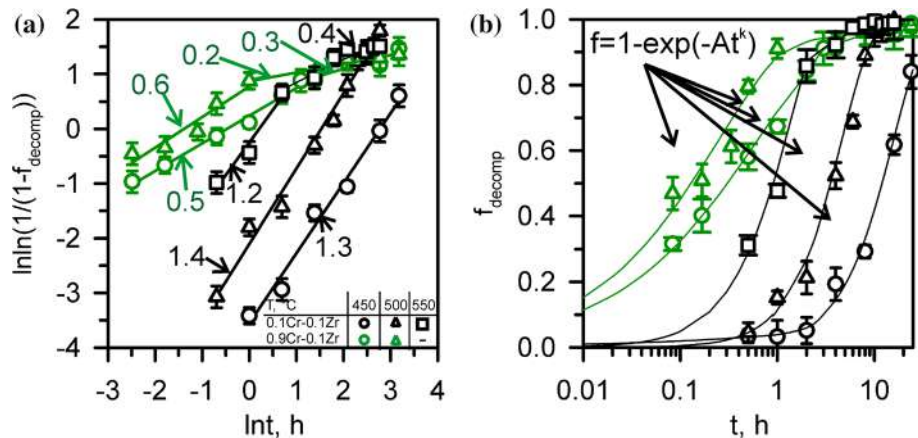
1.2 (close to k for 450–500 °C) for relatively short aging time and 0.4 for prolonged aging. Both relationships for the 0.9Cr–0.1Zr alloy aged at 450 and 500 °C have two slopes with k of 0.5–0.6 for short aging and 0.2–0.3 for a long time. A decrease in the slope at an early aging in the 0.9Cr–0.1Zr alloy in comparison with the 0.1Cr–0.1Zr alloy is associated with acceleration of the decomposition of solid solution. Note that the incubation period of the decomposition of supersaturated solid solution decreases with increasing Cr content and aging temperature. A coefficient A in the 0.9Cr–0.1Zr alloy is larger than that in the 0.1Cr–0.1Zr alloy by 44 and 19 times after aging at 450 and 500 °C, respectively.

An increase in the aging temperature significantly accelerates the decomposition of the supersaturated solid solution. The following relationship between the time for a specific fraction of decomposition (the time for 50% decomposition, $t_{0.5}$, is commonly used) and the aging temperature can be used to evaluate the rate of decomposition [52, 53].

$$1/t_{0.5} = A_0 \exp\left(-\frac{Q}{R*T}\right), \qquad (6)$$

where A_0 is a constant, Q is the activation energy of the decomposition process that can be estimated by plotting $\ln 1/t_{0.5}$ vs $1/T$, $R*$ is a gas constant. The activation energy for the decomposition of solid solution of 128 kJ/mole was obtained for the present 0.1Cr–0.1Zr alloy. This value is close to the activation energy of Zr diffusion in Cu (127 kJ/mole [54]), suggesting that Zr diffusion controls the decomposition in the 0.1Cr–0.1Zr alloy during aging at 450–550 °C. On the other hand, a relatively low value of 67 kJ/mole was observed for the decomposition activation energy for the 0.9Cr–0.1Zr alloy. Such

apparently low value of activation energy may reflect the rapid kinetics of the precipitation process similar to continuous decompositions [53, 55].

It is clearly seen in Figs. 1b, d and 7a that the decomposition kinetics with a slope above 0.5 corresponds to the quick increase in the electrical conductivity at an early aging stage and can be associated with the particle nucleation and rapid growth owing to solute depletion. Further aging with a slope of 0.2–0.4 in Fig. 7a corresponds to Orowan ripening. The particle sizes after the same aging treatment in the 0.1Cr–0.1Zr and 0.9Cr–0.1Zr alloys are different (cf. Figures 3 and 4). The size of the fine Cr particles after aging at 500 °C during 16 h in the 0.1Cr–0.1Zr alloy is more than three times larger than that in the 0.9Cr–0.1Zr alloy (22.5 and 6.5 nm). The long incubation period of precipitation, the low number density and relatively large size of Cr-particles in the 0.1Cr–0.1Zr alloy can be associated with the change of the driving force of particle precipitation Δg with Cr content in a copper alloy in accordance with the following relationship [56]:

$$\Delta g = -\frac{kT}{v_{at}}\ln^2(C/C_{eq}), \qquad (7)$$

where k is the Boltzmann constant (1.38×10^{-23} J K^{-1}), T is the aging temperature in K, v_{at} is the atomic volume, C is the current solute concentration of the matrix, C_{eq} is the equilibrium solute concentration of the matrix.

According to Eq. (6), the driving force of precipitation after solution treatment in the 0.1Cr–0.1Zr alloy is about 2.3 times lower than in the 0.9Cr–0.1Zr alloy. The driving force is determined by the concentration of alloying elements in solid solution and

controls the particle nucleation rate (dN/dt) and the growth rate (dR/dt) as follows [56]:

$$\frac{dN}{dt} = \frac{1}{v_{at}} Z\beta \exp\left(-\frac{\Delta G}{kT}\right)\left(-\frac{\tau}{t}\right), \tag{8}$$

where

$$\beta = \frac{4\pi R_0^2 DC}{a^4 \ln^2(C/C_{eq})}, \tag{9}$$

$$\Delta G = \frac{4\pi R_0^2 \gamma}{3\ln^2(C/C_{eq})}, \tag{10}$$

$$R_0 = \frac{2\gamma v_{at}}{kT}, \tag{11}$$

$$\tau = \frac{1}{2\beta Z}, \tag{12}$$

$$dR/dt = \frac{D}{R}\frac{C - C_{eq}\exp(R_0/R)}{1 - C_{eq}\exp(R_0/R)}, \tag{13}$$

Here v_{at} is the atomic volume for particle (volume of the Cr cell divided by the number of atoms in a cell, 1.2×10^{-29} m^3), Z is the Zeldovich factor (0.05), ΔG is the nucleation energy, τ is the incubation period of nucleation, t is the aging time, D is the diffusivity (2.63×10^{-17} m^2 h^{-1} for 450 °C [54]), C is the current concentration of solute atoms in the matrix, a is the lattice parameter of particles (2.885 nm), R is the current particle radius, R_0 is the critical nucleation radius, C_0 is the initial concentration of solute atoms in the matrix (0.001 for 0.1Cr–0.1Zr alloy and 0.0035 for 0.9Cr–0.1Zr alloy [57]), C_{eq} is the equilibrium solute concentration of the matrix (0.0001 [57]), γ is the particle interface energy.

The difference in the incubation period and the rate of solid solution decomposition in copper alloys may result from the competition between the rate of particle precipitation and particle growth depending on Cr content. In general, the high nucleation rate and the low growth rate lead to the fine particle precipitation with high number density. Opposite, the low nucleation rate and the high growth rate result in rare coarse particles [55]. According to Eqs. (7) and (8), an increase in Cr content and aging temperature lead to a decrease in the activation energy for nucleation. Thus, the particle nucleation accelerates and the incubation period of precipitation reduces.

Figure 8a illustrates the change in the nucleation rate during aging at 450 °C in the 0.1Cr–0.1Zr and 0.9Cr–0.1Zr alloys according to Eq. (8). The particle interface energy of 0.34 J m^{-2}, which is close to those of about 0.625 J m^{-2} [8] and 0.25 J m^{-2} [58], was determined from the experiment. The concentration of Cr in solid solution was estimated experimentally using Eqs. (4) and (5). The particle size is taken from Fig. 6. The maximal nucleation rate in the 0.1Cr–0.1Zr alloy (5.3^{19} h^{-1}) is significantly smaller than in the 0.9Cr–0.1Zr alloy (2.7^{21} h^{-1}) and located at longer aging times that is associated with both slow nucleation and small number density of the particles. The relationship between the particle growth rate and aging time is shown in Fig. 8b. The particle precipitation in the 0.9Cr–0.1Zr alloy at aging beginning leads to a decrease in the particle growth rate. Therefore, the change of the particle radius occurs faster in the 0.1Cr–0.1Zr alloy after 1 h aging despite the initial large concentration gradient in the 0.9Cr–0.1Zr alloy. Sheibani et al. [59] suggested a possibility of continuous spinodal decomposition in a type of Cu–Cr alloy resulting in reduced activation energy of nucleation and increased particle stability against coarsening during the aging. In contrast, the relatively large Cr particles in the 0.1Cr–0.1Zr alloy precipitate by conventional discontinuous decomposition.

The kinetics of Ostwald ripening is controlled by the interface energy (γ) of particles as follows [55, 56]:

$$R^3 - R_{nucl}^3 \propto \gamma Dt, \tag{14}$$

Here R_{nucl} is the nucleus radius. In turn, the interface energy depends on the misfit between the corresponding matrix and particle crystal planes (Table 1). The small misfit for N–W OR provides low-energy coherent interfaces for fine particles in the 0.9Cr–0.1Zr alloy. Thus, stabilizing the particle size in the 0.9Cr–0.1Zr alloy during aging is provided by a high nucleation rate and a low rate of particle growth, which is determined by the coherent interface boundary. On the other hand, Bain OR with the large misfit results in semi-coherent particles with a relatively high interface energy in the 0.1Cr–0.1Zr alloy. A relatively high energy of the semi-coherent interface boundaries in the 0.1Cr–0.1Zr alloy promotes the coarsening of Cr particles.

Therefore, the decomposition of solid solution in the 0.1Cr–0.1Zr alloy is controlled by the growth rate of particles with low number density and characterized by the high activation energy, the long incubation period of nucleation, and high growth rate. In contrast, the fast precipitation in the 0.9Cr–0.1Zr alloy owing to high concentration gradient results in the

Figure 8 Nucleation (**a**) and growth rate (**b**) of Cr-particles during aging at a temperature of 450 °C in the 0.1Cr–0.1Zr (black lines) and 0.9Cr–0.1Zr (green lines) alloys.
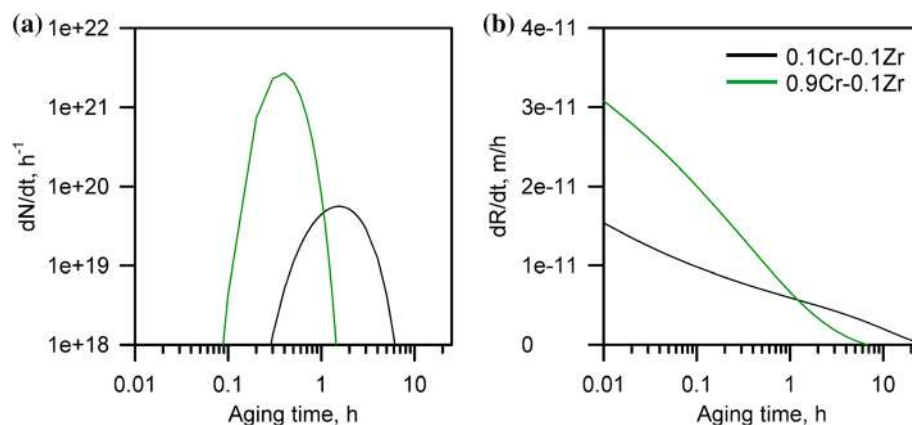
Table 1 Misfits for interfaces between bcc-Cr particle and Cu matrix

OR	Coincident planes/interplanar distances in Cu	Coincident planes/interplanar distance in Cr,	Misfit, $\Delta d/d$
Bain			
$(100)_{Cu}(100)_{Cr}$	{200}/0.1808 nm	{200}/0.1442 nm	0.225
$[010]_{Cu}[01-1]_{Cr}$	{200}/0.1808 nm	{110}/0.2039 nm	0.12
Nishiyama–Wassermann			
$(111)_{Cu}(1-10)_{Cr}$	{111}/0.2087 nm	{110}/0.2039 nm	0.023
$[-112]_{Cu}[10-1]_{Cr}$	3 × {211}/0.2214 nm	{110}/0.2039 nm	0.082
	{220}/0.1278 nm	{200}/0.1442 nm	0.121

rapid particle nucleation with high number density followed by a sluggish growth after 1 h aging.

Strengthening of copper alloys

In general, the yield strength of dispersion-hardened metallic materials can be estimated by a modified Hall–Petch relationship (Eq. 2). The lattice friction or Peierls–Nabarro stress for pure copper is $\sigma_0 = 25$ MPa [60]. The strengthening owing to the dislocation density, ρ, can be expressed as follows [47, 48]:

$$\sigma_\rho = \alpha M G b \sqrt{\rho}, \tag{15}$$

where α is a numerical factor of about 0.24 [61], M is the Taylor factor ($M = 3.06$ as determined from the EBSD data in the present study), $G = 42.1$ GPa is the shear modulus for pure copper [62], $b = 0.25$ is the Burgers vector [62]. The low dislocation densities of 3.8×10^{12} and 4.5×10^{11} m^{-2} in the 0.1Cr–0.1Zr and 0.9Cr–0.1Zr alloys, respectively, result in rather low dislocation strengthening of about 10 MPa. The investigated copper alloys are characterized by relatively large grain sizes of 12 µm in the 0.9Cr–0.1Zr

alloy and 125 µm in the 0.1Cr–0.1Zr alloy. Taking $k_y = 0.14$ MPa m$^{0.5}$ [62], the grain size strengthening comprises 10–30 MPa. Therefore, the last term in Eq. (2) does not significantly contribute to the yield strength. The main attention will be paid to the precipitation strengthening as the main contributor to the yield strength in dispersion-hardened alloys. The precipitation strengthening by the Orowan mechanism can be estimated by the modified Orowan equation [61]:

$$\sigma_{modOR} = M \frac{0.4 G b \ln(2R/b)}{\pi \lambda \sqrt{1-v}}, \tag{16}$$

with the interparticle spacing, $\lambda = 1.77 r/f^{1/2}$ [63], and the Poisson coefficient of $v = 0.35$. The volume fraction of particles was estimated using Eq. (4) as $f = f_{decomp} \times f_{max}$. The maximum volume fraction of Cr particles, f_{max}, was calculated for bcc Cr considering the limit of Cr solution in copper matrix that comprises 0.0012 in the 0.1Cr–0.1Zr alloy and 0.005 for the 0.9Cr–0.1Zr one. Calculation using Eq. (16) gives $\sigma_{mod\,OR} = 314$ MPa for the 0.9Cr–0.1Zr alloy aged at 450 °C for 4 h and $\sigma_{mod\,OR} = 82$ MPa for the 0.1Cr–0.1Zr alloy aged at 450 °C for 16 h (Table 2). Thus, the

Table 2 The strengthening contribution to the yield strength of 0.9Cr–0.1Zr and 0.1Cr–0.1Zr alloys

Alloy	Aging temperature (°C)	The lattice friction stress σ_0(MPa)	The grain boundary strengthening $k_y d^{-0.5}$, (MPa)	The dislocation strengthening $\alpha MGb\sqrt{\rho}$ (MPa)	The modified Orowan strengthening σ_{modOR} (MPa)	The particle strengthening by shear σ_{shear}(MPa)	The experimental yield strength σ_{YS_exp} (MPa)
0.1Cr–	450	25	13	15	82	1958	130
0.1Zr	500	25	13	15	51	3761	105
0.9Cr–	450	25	40	5	314	161	215
0.1Zr	500	25	40	5	233	205	215

modified Orowan equation gives closer calculated σ_{YS} to the experimental data, especially for the 0.1Cr–0.1Zr alloy aged at various temperatures, although the same calculation for the 0.9Cr–0.1Zr alloy seems to be inappropriate.

It is well known that the operating mechanism of precipitation strengthening depends on the stress, which is necessary for dislocation to overcome obstacles in the form of particles. It is clear from Table 2 that the mechanism of precipitation strengthening for 0.9Cr–0.1Zr should be different from the bowing dislocation between particles. When the dislocations overcome the dispersed particles by shear, the main contributors to the precipitation strengthening are coherency strengthening and modulus strengthening. The former can be estimated as follows [61]:

$$\sigma_{hoc} = M\varphi(2/3G\varepsilon)^{3/2}\left(\frac{Rf}{0.5Gb}\right)^{1/2} \tag{17}$$

where $\phi = 2.6$ is a constant, ε is the lattice misfit parameter. The modulus strengthening could be evaluated as [61]:

$$\sigma_G = M0.0055(\Delta G)^{3/2}(2f/G)^{0.5}(R/b)^{(3m/2)-1}. \tag{18}$$

To calculate the overall precipitation strengthening σ_{shear}, the different mechanisms are superimposed according to [47]:

$$\sigma_{shear} = \sqrt{\sigma_{coh}^2 + \sigma_G^2}, \tag{19}$$

The yield strength of the 0.9Cr–0.1Zr alloy aged at 450 °C for 4 h was calculated using Eqs. (16–19) to be 231 MPa, which is reasonably consistent with the experimental data (Table 2). In contrast, the application of the shearing mechanism to the 0.1Cr–0.1Zr

alloy results in overestimated values of the yield strength (Table 2).

Thus, the shearing mechanism of precipitation strengthening can be applied for the 0.9Cr–0.1Zr alloy, whereas particles in the 0.1Cr–0.1Zr alloy are overcome by the Orowan mechanism. The tiny Cr-rich coherent particles with a size of about 4–5 nm and a high volume fraction (Fig. 5) provide significant particle strengthening of more than 150 MPa. On the other hand, the Orowan strengthening from relatively large Cr-particles (8–10 nm) in the 0.1Cr–0.1Zr alloy (Fig. 3) comprises 60–85 MPa.

Conclusions

The aging behavior and the dispersion strengthening were studied in the 0.9Cr–0.1 Zr and 0.1Cr–0.1Zr copper alloys annealed at 450–550 °C for 0.5–16 h. The main results can be summarized as follows.

1. The kinetic of decomposition of solid solution and the size of the Cr particles depend on the Cr content, temperature, and aging time. The 0.9Cr–0.1Zr alloy is characterized by faster kinetic of particles precipitation, smaller Cr particles (particle size of 3–7 nm) with N–W OR than the 0.1Cr–0.1Zr alloy (particle size of 4–25 nm) with Bain OR at all temperatures/times.

2. The decomposition of solid solution in the 0.1Cr–0.1Zr alloys is controlled by the growth rate of particles with low number density and the nucleation activation energy equal to Zr diffusion, and characterized by the long incubation period of nucleation and high growth rate. Opposite, the fast depleting Cr from the matrix in the 0.9Cr–0.1Zr alloy due to high concentration

gradient results in quick precipitation of particles with the high number density at early aging and a decrease in particle growth rate after 1 h aging.

3. The 0.9Cr–0.1Zr alloy is characterized by more than 100 MPa increment in UTS in peak aged conditions compared with a solution-treated state, whereas the increment in UTS for 0.1Cr–0.1Zr alloy comprises 45–50 MPa.

4. The different strengthening mechanisms operate in the 0.1Cr–0.1Zr and 0.9Cr–0.1Zr alloys. The Orowan model is acceptable for the precipitation strengthening in the 0.1Cr–0.1Zr alloy. In contrast, the precipitation strengthening occurs through the shearing mechanism in the 0.9Cr–0.1Zr alloy. Relatively fine particles in the 0.9Cr–0.1Zr alloy with coherent boundaries are sheared by moving dislocations, whereas the coarse particles in the 0.1Cr–0.1Zr alloy with semi-coherent boundaries are overcome by an Orowan-type mechanism.

Authors contribution statement

AB and RM were involved in investigation. AB and AB were involved in data curation and writing—original draft. RM was involved in formal analysis and methodology. RK collected resources and performed supervision and project administration.

Declarations

Conflict of interest The authors declare that they have no known competing financial interests or personal relationships that could have appeared to influence the work reported in this paper.

References

[1] Tang NY, Taplin DMR, Dunlop GL (1985) Precipitation and aging in high-conductivity Cu–Cr alloys with additions of zirconium and magnesium. Mater Sci Technol 1:270–275. https://doi.org/10.1179/mst.1985.1.4.270

[2] Batra IS, Dey GK, Kulkarni UD, Banerjee S (2001) Microstructure and properties of a Cu–Cr–Zr alloy. J Nucl Mater 299:91–100. https://doi.org/10.1016/S0022-3115(01)00691-2

[3] Fuxiang H, Jusheng M, Honglong N, Zhiting G, Chao L, Shumei G, Xuetao Y, Tao W, Hong L, Huafen L (2003) Analyses of phases in a Cu–Cr–Zr alloy. Scr Mater 48:97–102. https://doi.org/10.1016/S1359-6462(02)00353-6

[4] Bodyakova A, Pilipenko A, Lugovskaya A, Belyakov A, Kaibyshev R (2021) Thermal stability of gradient microstructure in a low-alloyed Cu-Cr-Zr alloy. Mater Lett 304:130531. https://doi.org/10.1016/j.matlet.2021.130531

[5] Purcek G, Yanar H, Demirtas M, Shangina DV, Bochvar NR, Dobatkin SV (2020) Microstructural, mechanical and tribological properties of ultrafine-grained Cu–Cr–Zr alloy processed by high pressure torsion. J All Comp 816:152675. https://doi.org/10.1016/j.jallcom.2019.152675

[6] Aksenov DA, Raab GI, Asfandiyarov RN, Semenov VI, Shuster LS (2020) Effect of Cd and SPD on structure, physical, mechanical, and operational properties of alloy of Cu-Cr-Zr. Rev Adv Mater Sci 59(1):506–513. https://doi.org/10.1515/rams-2020-0045

[7] Morozova AI, Belyakov AN, Kaibyshev RO (2021) Effect of deformation temperature on formation of ultrafine-grained structure in the age-hardenable Cu–Cr–Zr alloy. Phys Metals Metallog 122(1):60–66. https://doi.org/10.1134/S0031918X21010087

[8] Chibihi A, Sauvage X, Blavette D (2012) Atomic scale investigation of Cr precipitation in copper. Acta Mater 60:4575–4585. https://doi.org/10.1016/j.actamat.2012.01.038

[9] Lin GB, Wang ZD, Zhang MK, Zhang H, Zhao M (2011) Heat treatment method for making highstrength and conductivity Cu–Cr–Zr alloy. Mater Sci Technol 27:966–969. https://doi.org/10.1179/026708310X12815992418210

[10] Zhilyaev AP, Morozova A, Cabrera JM, Kaibyshev R, Langdon TG (2017) Wear resistance and electroconductivity in a Cu–0.3 Cr–0.5 Zr alloy processed by ECAP. J Mater Sci 52(1):305–313. https://doi.org/10.1007/s10853-016-0331-8.

[11] Peng H, Xie W, Chen H, Wang H, Yang B (2021) Effect of micro-alloying element Ti on mechanical properties of Cu–Cr alloy. J All Comp 852:157004. https://doi.org/10.1016/j.jallcom.2020.157004

[12] Huang Z, Shi R, Xiao X, Fu H, Chen Q, Xie J (2021) Mechanism investigation on high-performance Cu-Cr-Ti alloy via integrated computational materials engineering. Mater Today Com 27:102378. https://doi.org/10.1016/j.mtcomm.2021.102378

[13] Sun Y, Peng L, Huang G, Xie H, Mi X, Liu X (2020) Effects of Mg addition on the microstructure and softening resistance of Cu–Cr alloys. Mater Sci Eng A 776: 139009. https://doi.org/10.1016/j.msea.2020.139009.

[14] Zeng H, Sui H, Wu S, Liu J, Wang H, Zhang J, Yang B (2021) Evolution of the microstructure and properties of a Cu–Cr-(Mg) Alloy upon thermomechanical treatment. J All Comp 857:157582. https://doi.org/10.1016/j.jallcom.2020.157582

[15] Fujii T, Nakazawa H, Kato M, Dahnem U (2000) Crystallography and morfology of nanosized Cr particles in a Cu–0.2%Cr alloy. Acta Mater 48:1033–1045. https://doi.org/10.1016/S1359-6454(99)00411-5

[16] Correia JB, Davies HA, Sellars CM (1997) Strengthening in rapidly solidified and hardened Cu–Cr and Cu–Cr–Zr alloys. Acta Mater 45:177–190. https://doi.org/10.1016/S1359-6454(96)00142-5

[17] Singh RP, Lawley A, Friedman S, Murty YV (1991) Microstructure and properties of spray cast Cu-Zr alloys. Mater Sci Eng A 145:243–255. https://doi.org/10.1016/0921-5093(91)90254-K

[18] Peng L, Xie H, Huang G, Li Y, Yin X, Feng X (2015) The phase transformation and its effects on properties of a Cu–0.12 wt% Zr alloy. Mater Sci Eng A 145:28–34. https://doi.org/10.1016/j.msea.2015.02.077

[19] Zel'dovich VI, Dobatkin SV, Frolova NY, Khomskaya IV, Kheifets AE, Shorokhov EV, Nasonov PA (2016) Mechanical properties and the structure of chromium–zirconium bronze after dynamic channel-angular pressing and subsequent aging. Phys Metals Metallog 117(1):74–82. https://doi.org/10.1134/S0031918X16010129

[20] Wang K, Liu K-F, Zhang J-B (2014) Microstructure and properties of aging Cu–Cr–Zr alloy. Rare Met 33:134–138. https://doi.org/10.1007/s12598-014-0244-0

[21] Cheng JY, Shen B, Yu FX (2013) Precipitation in a CuCrZrMg alloy during aging. Mater Character 81:68–75. https://doi.org/10.1016/j.matchar.2013.04.008

[22] Williams RO (1960) Precipitation process in Cu-Cr alloys. Trans ASM 52:530–538

[23] Knights RW, Wilkes P (1973) Precipitation of chromium in copper and copper-nickel base alloys. Metall Trans 4:2389–2393. https://doi.org/10.1007/BF02669380

[24] Weatherly GC, Humble P, Borland D (1979) Precipitation in a Cu–0.55wt%Cr alloy. Acta Mater 27:1815–1828. https://doi.org/10.1016/0001-6160(79)90072-5

[25] Zhou HT, Zhong JW, Zhou X, Zhao ZK, Li QB (2008) Microstructure and properties of Cu–1.0Cr–0.2Zr–0.03Fe alloy. Mater Sci Eng A 498:225–230. https://doi.org/10.1016/j.msea.2008.07.061

[26] Kawakatsu I, Suzuki H, Kitano H (1967) Properties of high zirconium copper-zirconium-chromium alloys and isothermal diagram at the copper-rich corner. J Jpn Inst Met 31:1253–1257

[27] Holzwarth U, Stamm H (2000) The precipitation behaviour of ITER-grade Cu-Cr-Zr alloyafter simulating the thermal cycle of hot isostatic pressing. J Nucl Mater 279:31–45. https://doi.org/10.1016/S0022-3115(99)00285-8

[28] Lou MYW, Grant NJ (1984) Identification of Cu5Zr phase in Cu-Zralloys. Metall Trans A 15:1491–1493

[29] Watanabe C, Monzen R, Tazaki K (2008) Mechanical properties of Cu–Cr system alloys with and without Zr and Ag. J Mater Sci 43:813–819. https://doi.org/10.1007/s10853-007-2159-8

[30] Vitek JM (1976) Ellectron microprobe investigation of the intermediate phases in the Cu-Zr system. Z Metallkd 67:559–563. https://doi.org/10.1515/ijmr-1976-670810

[31] Chembarisova RG, Galaktionova AV, Yamileva AM (2021) Evolution of Secondary Phase Particles in Cu–Cr–Zr Alloys with an extremely low concentration of solid solution during thermomechanical treatment. Phys Metals Metallog 122(1):40–46. https://doi.org/10.1134/S0031918X21010026

[32] Donachje MJ (1963) Investigation of copper-rich portion of copper-zirconium phase diagram by electron-probe microanalysis. J Inst Met 92:180–185

[33] Su JH, Liu P, Li HJ, Ren FZ, Dong QM (2007) Phase transformation in Cu–Cr–Zr–Mg alloy. Mater Lett 61:4963–4966. https://doi.org/10.1016/j.matlet.2007.03.085

[34] Su JH, Dong QM, Liu P, Li HJ, Kang BX (2005) Research on aging precipitation in a Cu–Cr–Zr–Mg alloy. Mater Sci Eng A 392:422–426. https://doi.org/10.1016/j.msea.2004.09.041

[35] Mu SG, Guo FA, Tang YQ, Cao XM, Tang MT (2008) Study on microstructure and properties of agedCu–Cr–Zr–Mg–RE alloy. Mater Sci Eng A 475:235–240. https://doi.org/10.1016/j.msea.2007.04.056

[36] Wang J, Zhang HT, Fu HD, Xie JX (2021) Effect of Cr content on microstructure and properties of aged Cu–Cr–P

alloys. Trans Nonfer Met Soc China 31(1):232–242. https://doi.org/10.1016/S1003-6326(20)65490-5

[37] Zel'dovich VI, Dobatkin SV, Frolova NY, Khomskaya IV, Kheifets AE, Shorokhov EV, Nasonov PA (2016) Mechanical properties and the structure of chromium–zirconium bronze after dynamic channel-angular pressing and subsequent aging. Phys Metal Metallog 117(1):74–82. https://doi.org/10.1134/S0031918X16010129

[38] Khomskaya IV, Zel'Dovich VI, Shorokhov EV, Frolova NY, Kheifets AE, Dyakina VP (2017) Effect of high-rate deformation on the structure, the properties, and the thermal stability of copper alloyed with chromium and zirconium. Rus Metallurg (Metally) 10:851–857. https://doi.org/10.1134/S003602951710010X

[39] Morozova A, Mishnev R, Belyakov A, Kaibyshev R (2018) Microstructure and properties of fine grained Cu-Cr-Zr alloys after termo-mechanical treatments. Rev Adv Mater Sci 54(1):56–92. https://doi.org/10.1515/rams-2018-0020

[40] Ahmadi MR, Sonderegger B, Povoden-Karadeniz E, Falahati A, Kozeschnik E (2014) Precipitate strengthening of non-spherical precipitates extended in <100> or 100 direction in fcc crystals. Mater Sci Eng A 590:262–266. https://doi.org/10.1016/j.msea.2013.10.043

[41] Sonderegger B, Kozeschnik E (2012) Particle strengthening in fcc crystals with prolate and oblate precipitates. Scr Mater 66:52–55. https://doi.org/10.1016/j.scriptamat.2011.10.003

[42] Kendig KL, Miracle DB (2002) Strengthening mechanisms of an Al-Mg-Sc-Zr alloy. Acta Mater 50:4165–4175. https://doi.org/10.1016/S1359-6454(02)00258-6

[43] Hull D, Bacon DJ (1984) Introduction to dislocations, 3rd edn. Pergamon Press, Oxford

[44] Ahmadi MR, Povoden-Karadeniz E, Whitmore L, Stockinger M, Falahati A, Kozeschnik E (2014) Yield strength prediction in Ni-base alloy 718Plus based on thermo-kinetic precipitation simulation. Mater Sci Eng A 608:114–122. https://doi.org/10.1016/j.msea.2014.04.054

[45] Nembach F (1983) Precipitation hardening caused by a difference in shear modulus between particle and matrix. Phys Stat Solid A 78:571–581. https://doi.org/10.1002/pssa.2210780223

[46] Kocks UF, Mecking H (2003) Physics and phenomenology of strain hardening: the FCC case. Prog Mater Sci 48:171–273. https://doi.org/10.1016/S0079-6425(02)00003-8

[47] Holzner I, Kozeschnik E (2010) Computer simulation of the yield strength evolution in Cu-precipitation strengthened ferritic steel. Mater Sci Eng A 527:3546–3551. https://doi.org/10.1016/j.msea.2010.02.032

[48] Ahmadi MR, Povoden-Karadeniz E, Oksuz KI, Falahati A, Kozeschnik E (2014) A model for precipitation strengthening in multi-particle systems. Comp Mater Sci 91:173–186. https://doi.org/10.1016/j.commatsci.2014.04.025

[49] Buschow KV, Van Engen PG, Jongebreur R (1983) Magneto-optical properties of metallic ferromagnetic materials. J Magn Magn Mater 38(1):1–22. https://doi.org/10.1016/0304-8853(83)90097-5

[50] Matthiessen A, Vogt C (1864) IV. On the influence of temperature on the electric conducting-power of alloys. Philos Trans R Soc 154 (1864):167–200. https://doi.org/10.1098/rstl.1864.0004.

[51] Su J, Liu P, Li H, Ren F, Dong Q (2007) Phase transformation in Cu–Cr–Zr–Mg alloy. Mater Let 61(27):4963–4966. https://doi.org/10.1016/j.matlet.2007.03.085

[52] Wang J, Kou HC, Gu XF, Li J S, Xing L Q, Hu R, Zhou L (2009) On discussion of the applicability of local Avrami exponent: errors and solutions. Mater Let 63(13–14):1153–1155. https://doi.org/10.1016/j.matlet.2009.01.027

[53] Li Y, Yang B, Zhang P, Ni Y, Yuan X, Le Q, Li Y (2021) Cu-Cr-Mg alloy with both high strength and high electrical conductivity manufactured by powder metallurgy process. Mater Today Com 27:102266. https://doi.org/10.1016/j.mtcomm.2021.102266

[54] Butrymowicz DB, Manning JR, Read ME (1975) Diffusion in copper and copper alloys. Part III. Diffusion in systems involving elements of the groups IA, IIA, IIIB, IVB, VB, VIB, and VIIB. J Phys Chem Ref Data 4(1):177–250. https://doi.org/10.1063/1.555516.

[55] Gottstein G (2004) Physical foundations of materials science, 1st edn. Springer-Verlag, Berlin

[56] Deschamps A, Brechet Y (1998) Influence of predeformation and ageing of an Al–Zn–Mg alloy—II. Modeling of precipitation kinetics and yield stress. Acta Mater 47(1):293–305. https://doi.org/10.1016/S1359-6454(98)00296-1.

[57] Lyakishev NP, Bannykh OA (1996) Phase diagrams of binary metallic systems: a handbook, 1st edn. Mechanical Engineering, Moscow

[58] Wu S, Wang J, Zhong S, Zhang J, Wang H, Yang B (2019) Effect of trace Mg addition on precipitation behavior and properties of Cu-Cr alloy. Chin J Mater Res 33(7):552–560. https://doi.org/10.11901/1005.3093.2018.596.

[59] Sheibani S, Heshmati-Manesh S, Ataie A, Caballero A, Criado JM (2014) Spinodal decomposition and precipitation in Cu–Cr nanocomposite. J All Comp 587:670–676. https://doi.org/10.1016/j.jallcom.2013.11.019

[60] Smith WF, Hashemi J (2003) Foundations of materials science and engineering. McGraw-Hill, New York (USA)

[61] Harrell TJ, Topping TD, Wen H, Hu T, Schoenung JM, Lavernia EJ (2014) Microstructure and strengthening

mechanisms in an ultrafine grained Al-Mg-Sc alloy produced by powder metallurgy. Metal Mater Trans A 45(13):6329–6343. https://doi.org/10.1007/s11661-014-2569-6

[62] Schneibel JH, Heilmaier M (2014) Hall-Petch breakdown at elevated temperatures. Mater Trans 55(1):44–51. https://doi.org/10.2320/matertrans.MA201309

[63] Russell KC, Brown LM (1972) A dispersion strengthening model based on differing elastic moduli applied to the iron-copper system. Acta Metall 20(7):969–974. https://doi.org/10.1016/0001-6160(72)90091-0